

Examining Brightness Variability, Accretion Disk and Evolutionary Stage of Binary OGLE-LMC-ECL-14413

R.E. Mennickent¹, G. Djurašević^{2,3}, J.A. Rosales¹, J. Garcés¹, J. Petrović², D.R. G. Schleicher¹, M. Jurkovic², I. Soszyński⁴, and J.G. Fernández-Trincado⁵

¹ Universidad de Concepción, Departamento de Astronomía, Casilla 160-C, Concepción, Chile
e-mail: rmennick@udec.cl

² Astronomical Observatory, Volgina 7, 11060 Belgrade 38, Serbia

³ Issac Newton institute of Chile, Yugoslavia Branch, 11060, Belgrade, Serbia

⁴ Astronomical Observatory, University of Warsaw, Al. Ujazdowskie 4, 00-478 Warszawa, Poland

⁵ Instituto de Astronomía, Universidad Católica del Norte, Av. Angamos 0610, Antofagasta, Chile

Received XX XX, 2021; accepted XX XX, 2021

ABSTRACT

Context. Several intermediate-mass close binary systems exhibit photometric cycles longer than their orbital periods, potentially due to changes in their accretion disks. Past studies indicate that analyzing historical light curves can provide valuable insights into disk evolution and track variations in mass transfer rates within these systems.

Aims. Our study aims to elucidate both short-term and long-term variations in the light curve of the eclipsing system OGLE-LMC-ECL-14413, with a particular focus on the unusual reversals in eclipse depth. We aim to clarify the role of the accretion disk in these fluctuations, especially in long-cycle changes spanning hundreds of days. Additionally, we seek to determine the evolutionary stage of the system and gain insights into the internal structure of its stellar components.

Methods. We analyzed photometric time series from the Optical Gravitational Lensing Experiment (OGLE) project in I and V bands, and from the Massive Compact Halo Objects (MACHO) project in B_M and R_M bands, covering a period of 30.85 years. Using light curve data from 27 epochs, we constructed models of the accretion disk. An optimized simplex algorithm was employed to solve the inverse problem, deriving the best-fit parameters for the stars, orbit, and disk. We also utilized the Modules for Experiments in Stellar Astrophysics (MESA) software to assess the evolutionary stage of the binary system, investigating the progenitors and potential future developments.

Results. We found an orbital period of 38.15917 ± 0.00054 days and a long-term cycle of approximately 780 days. Temperature, mass, radius, and surface gravity values were determined for both stars. The photometric orbital cycle and the long-term cycle are consistent with a disk containing variable physical properties, including two shock regions. The disk encircles the more massive star and the system brightness variations aligns with the long-term cycle at orbital phase 0.25. Our mass transfer rate calculations correspond to these brightness changes. MESA simulations indicate weak magnetic fields in the donor star's subsurface, which are insufficient to influence mass transfer rates significantly.

Conclusions.

Key words. stars: binaries (including multiple), close, eclipsing - stars: variables: general - accretion: accretion disks

1. Introduction

Interacting binary stars constitute complex natural laboratories, allowing the study of a wide range of phenomena such as the physics of accretion disks, stellar winds, gas dynamics of mass flows between stars, angular momentum loss and balance, stellar rotation and the effects of tidal forces. It is believed that a significant portion of stars are members of multiple star systems, and that interactions between closely bound, gravitationally linked stars are common in the Universe. The most energetic phenomena detected so far, such as the merging of black holes or neutron stars, are considered to be the final stages in the evolution of binary systems that have previously undergone phases of mass transfer and angular momentum loss. A good review of binary star evolution is given by Eggleton (2011).

Among the myriad of interacting binary stars, a particularly intriguing group displays a photometric periodicity longer than the orbital period of typical amplitude at the I -band of 0.1 or 0.2 mag, whose nature still defies explanation (Mennickent et

al. 2003; Mennickent 2017). These are known as Double Periodic Variable stars (DPVs), with masses around 10 solar masses and orbital periods ranging from 3 to 100 days. In these systems, there is invariably a B-type dwarf star, enveloped in a gas disk fed by a cooler giant star of approximately one solar mass that fills its Roche lobe. More than 200 DPVs have been reported in the Galaxy and the Magellanic Clouds (Mennickent et al. 2003; Poleski et al. 2010; Pawlak et al. 2013; Mennickent, Otero & Kołaczkowski 2016; Rojas García et al. 2021) and the well studied systems reveal higher luminosities and hotter temperatures than normal Algol-type binaries (Mennickent, Otero & Kołaczkowski 2016). Some examples of these systems previously detected in our Galaxy include RX Cas (Gaposchkin 1944), AU Mon (Lorenzi 1980), β Lyr (Guinan 1989), V 360 Lac (Hill et al. 1997) and CX Dra (Koubsky et al. 1998).

It has been proposed that the longer period of DPVs results from variations in the mass transfer rate, modulated by oscillations in the equatorial radius of the donor star, governed by a magnetic dynamo cycle (Schleicher & Mennickent 2017). This

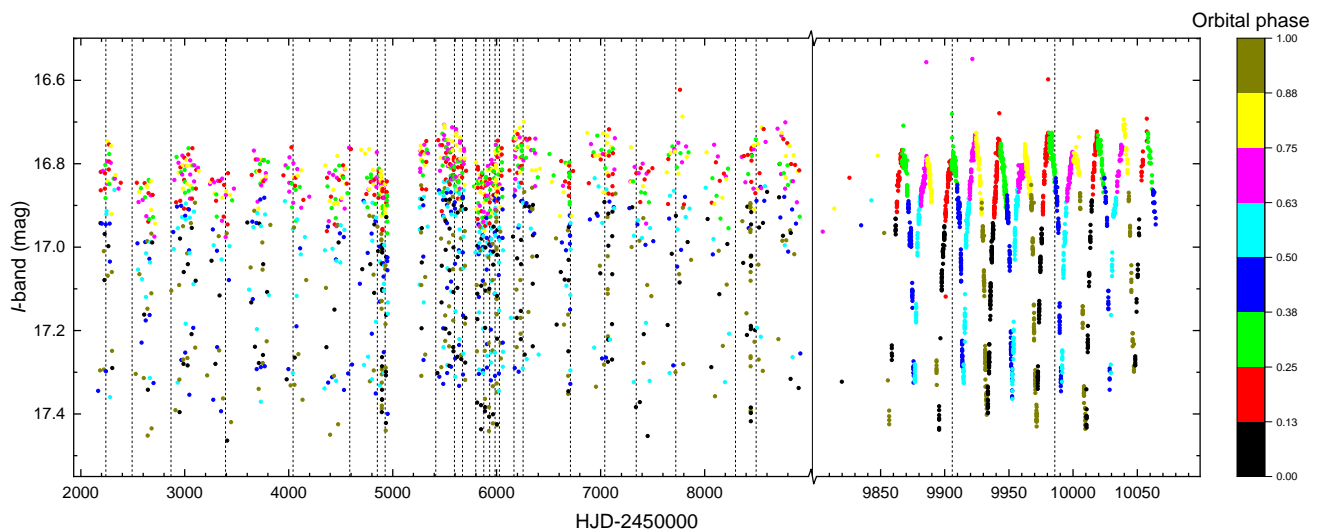


Fig. 1. OGLE I -band light curve of OGLE-LMC-ECL-14413. Colors indicate different orbital phases and dashed lines show mid times of the data strings listed in Table 2.

would induce observable changes in the gas disk over extended time scales. While few DPVs have been investigated with high levels of detail and precision, recent analyses of light curves from the Optical Gravitational Lensing Experiment (OGLE) database for specific objects have yielded intriguing insights.

For instance, OGLE-LMC-DPV-097 displays a notable long-term cycle length of ~ 306 days, with a significant fluctuation of ~ 0.8 magnitudes in the I -band. This system orbits every 7^d75 and comprises stars with modest masses of 5.5 and $1.1M_{\odot}$. A key finding from examining OGLE-LMC-DPV-097 is the systematic variation in its orbital light curve throughout the long-term cycle. At the long cycle's nadir, the secondary eclipse is almost imperceptible, and in the rising phase, the system's brightness is more pronounced in the first quadrant compared to the second. These observations can be attributed to the variations in the disk's temperature and dimensions, alongside fluctuations in the luminous and heated spots. The disk's radius contracts to $7.5 R_{\odot}$ at the cycle's low point and expands to $15.3 R_{\odot}$ during the rise, with its outer edge temperature varying from 6870 K to 4030 K between these phases (Garcés et al. 2018).

In examining the photometric characteristics of OGLE-BLG-ECL-157529, we encounter another intriguing scenario. This system is marked by orbital and extended periods of 24.8 days and 850 days, respectively, with stellar masses similar to OGLE-LMC-DPV-097. It is observed that while the primary minimum's magnitude remains largely stable, the secondary minimum exhibits significant fluctuations. The secondary minimum occurs due to the eclipse of the donor star by the combined structure of the accretor and its disk. This suggests the presence of a fluctuating accretion disk. Notably, the brightness at the orbital phase of 0.25 aligns closely with the long-term cycle. The disk's fractional radius (F_d), a metric for the accretor's Roche lobe occupancy, reveals that the disk expands beyond the tidal radius during peak activity and longer cycles. Conversely, F_d decreases below the tidal radius during quicker, less intense long-term cycles in later epochs. In this system, the long-term cycle's minimum is attributed to a thicker disk that obscures more of the accretor, with a higher mass transfer rate resulting in a hotter disk at the outer edge. The disk's radius oscillations over hundreds of days defy explanation through viscous energy release, as seen in the superhumps of precessing disks in cataclysmic variables like

Table 1. Photometric observations.

band	N	HJD' _{start}	HJD' _{end}	mean \pm std (mag)
B_M	1315	-1173.8652	1541.9973	-5.850 ± 0.175
R_M	1510	-1173.8652	1541.9973	-6.417 ± 0.173
I	535	2167.8681	4955.5136	16.985 ± 0.180
V	136	2994.7006	4955.4684	18.143 ± 0.180
I	3364	5260.6121	10064.5314	16.946 ± 0.182
V	280	5260.6596	10061.4713	18.111 ± 0.178

Note: Summary of OGLE-III, OGLE-IV and MACHO photometric observations analyzed in this paper. The number of measurements, starting and ending times, and average magnitude and their standard deviation are given. HJD' = HJD-2450000. The uncertainty of a single OGLE measurement varies between 4 and 6 mmag and for MACHO R_M and B_M are typically 0.048 mag and 0.058 mag.

SU UMa stars. This is because Lindblad resonance regions lie well outside the disk's radius. As an alternative, the hypothesis of variable mass injection as a cause for long-term photometric variability has been suggested (Mennickent & Djurašević 2021).

In order to complement the above studies, and provide a much complete picture of the behavior of these DPV systems, we present a photometric study of the eclipsing binary DPV OGLE-LMC-ECL-14413 (Graczyk et al. 2011; Pawlak et al. 2016). This binary is also known as OGLE-III LMC162.7.89414, OGLE-IV LMC503.02.14123, TIC 373520393, MACHO 78.6943.2764 and 2MASS J05232086-6950586 and their data include $\alpha_{2000}=05:23:20.96$, $\delta_{2000}=-69:50:58.0^1$ and $I=16.817$ mag and $V=18.001$ mag². This object was selected because of its relatively long orbital period and peculiar characteristics. The OGLE Collection of Variable Stars Website indicates that the system has an orbital period of $38^d1613814$. The system is mentioned as a unique DPV among the sample of LMC DPVs studied by Poleski et al. (2010). These authors noticed that apparently the amplitude of the long-term cycle gets smaller during one of the eclipses, also that the depth of the usually deeper minimum changes from cycle to cycle. They argue that a similar depth of both minima suggests that temperatures of both components are similar and conclude, from the observation that the mean light curve is typical for semi-detached or contact binary

¹ <https://gea.esac.esa.int/archive/>

² <https://simbad.cfa.harvard.edu/simbad/>

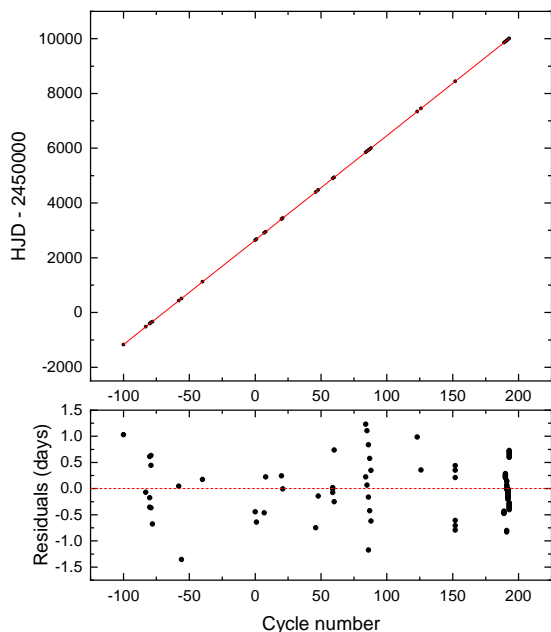


Fig. 2. Times of main minima versus cycle number and the best linear fit along with residuals. The slope of the fit gives the orbital period, viz. $P_o = 38^d15917 \pm 0^m00054$.

systems, that the radius of the donor star is one of the biggest among donors of known DPVs, or the total mass of the binary is smaller than for the other DPVs. The authors also argue that the donor eclipses the disk and the gainer during the shallower and more stable eclipse.

2. Photometric data and light curve

The photometric time series analyzed in this study consists of 3899 *I*-band data points and 416 *V*-band datapoints obtained by The Optical Gravitational Lensing Experiment (OGLE, Udalski, Szymański, & Szymański 2015). The *I*-band light curve shows the typical variability of an eclipsing binary, plus a long-term variability that is remarkable in the upper boundary of the dataset, that is shaped by the brighter datapoints (Fig. 1). In addition, we study 1315 B_M and 1510 R_M data points obtained by the Massive Compact Halo Objects (MACHO) project³. The whole dataset, summarized in Table 1, spans a time interval of 30.85 yr.

In this paper, as a starting point, we use the ephemeris for the occultation of the cooler star, provided by the OGLE team (Pawlak et al. 2016, no error is given):

$$\text{HJD} = 245\,7033^d527 + 38^d1613814\text{E}. \quad (1)$$

When comparing DPV systems that feature alternating depths of primary and secondary minima, it is crucial to maintain a consistent physical definition of these eclipses. As mentioned earlier, we have adhered to the methodology established by Pawlak et al. (2016).

In order to check the constancy of the orbital period, we performed an analysis of the times of the primary eclipse using the method of comparison of predicted times with observed times of eclipses, described by Sterken (2005). As eclipse timings we have chosen the fainter points in the colored data strings

shown in Fig. 1. We find that the data is compatible with a constant orbital period and there is no practical difference with the ephemerides provided by the OGLE team.

Furthermore, in order to improve the orbital period, we performed an analysis of the main eclipse times. For that, since most eclipses are not well defined individually, and after a visual inspection of the light curve, we selected candidates for minima as those observations with magnitudes at bands *I*, B_M and R_M fainter than 17.4, -5.35 and -6.00 and few outliers with phases discordant were rejected. The 95 eclipse times thus selected are shown in Table B.1.

Using the published orbital period as a trial, we calculated the cycle numbers for every minimum and fit a straight among the (N, time) pairs obtaining the following improved ephemeris for the main eclipse (Fig. 2):

$$\text{HJD} = 245\,2645^d198(83) + 38^d15917(54)\text{E}. \quad (2)$$

This new orbital period has a difference of 0^d00221 with the previously reported period, this accumulates 0^d66 during the 300 cycles of observations, or equivalently 0.017 orbital phase units. We also calculated the orbital period for the OGLE data yielding $P_o = 38^d159 \pm 0^m012$ using the Phase Dispersion Minimization software (PDM, Stellingwerf 1978) and $P_o = 38^d123 \pm 0^m095$ using the Generalized Lomb Scargle software (GLS, Zechmeister & Kürster 2009).

The light curve variability cannot be understood in terms of a two stars system, and the presence of circumstellar matter around the gainer is suggested by the observations (Fig. 3). It is interesting that the eclipse observed at phase 0.0, that sometimes is the deeper one, corresponds to occultation of the donor, since it is the eclipse with larger residuals and inter-epoch variability. The cooler star (the donor) is eclipsed by a variable physical structure. However, the depth of eclipse at phase 0.5 is rather stable, compatible with the stability of the donor and the occultation of the whole disk or a large fraction of it. The roughly constant shape of this eclipse confirms our ephemerides. Furthermore, there is no evidence for changes in the orbital period. The light curve outside the eclipse of the gainer, shows larger scatter before epochs at $\text{HJD}' \sim 8273$. On the other hand, at some epochs, the ingress of the eclipse of the donor is delayed, producing an eclipse of asymmetrical shape. These aspects could be attributed to variable amounts of circumstellar mass in the line of sight, considering the interacting nature of this binary discussed later in this paper.

While the *I*-band light curve is dense enough to allow a good analysis of orbital and system parameters, the *V*-band data are scarce, and we used them only for determination of the color at minimum and temperature of the donor star. During the secondary eclipse, the color $V - I = 1.263$ mag. If we take the mean $E(V - I) = 0.113 \pm 0.060$ mag for the LMC (Joshi & Panchal 2019), then we get $(V - I)_0 = 1.150 \pm 0.06$ mag, implying $T_2 = 5100$ K, according to the calibration given by Mennickent et al. (2020a). As a reference, the OGLE database provides $V - I = 1.156$ mag, suggesting $T_2 = 4982$ K, but this value rests on the average color from the entire light curve. We can also use the reddening maps by Skowron et al. (2021) to get $E(V - I) = 0.106 \pm 0.086$ which gives $(V - I)_0 = 1.157 \pm 0.086$ mag. We decided to keep fixed the temperature of the donor in $T_2 = 5000$ with an uncertainty of ± 200 K, neglecting errors that could come from the disk contribution to the color at the secondary eclipse.

³ <https://datacommons.anu.edu.au/DataCommons/item/anudc:3255>

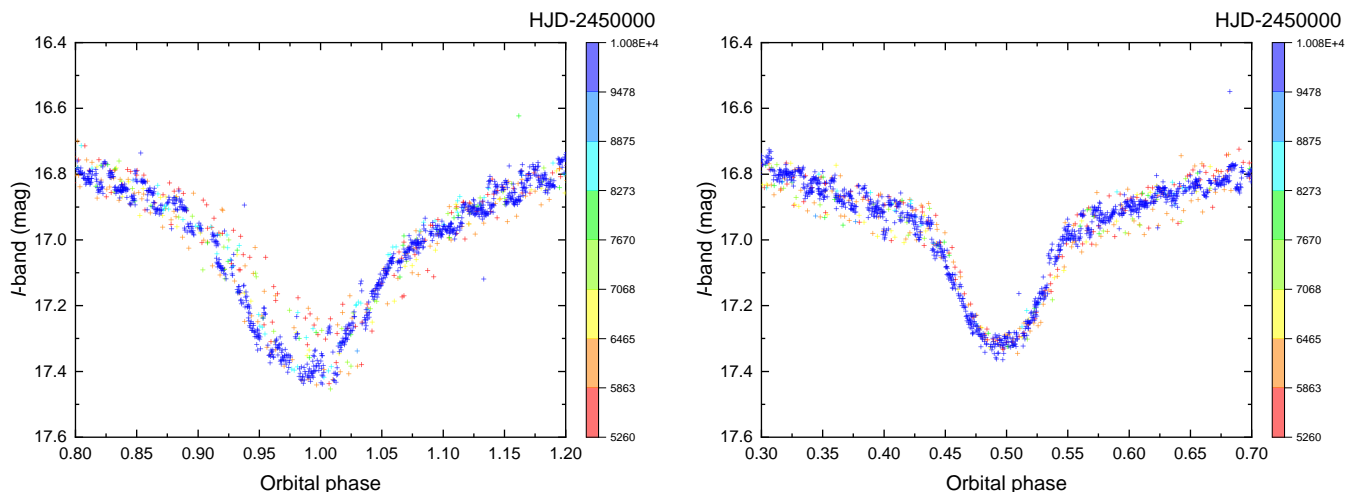


Fig. 3. OGLE *I*-band light curve of OGLE-LMC-ECL-14413 phased with the orbital period around the eclipse of the donor (left) and the gainer (right). Colors indicate different HJDs.

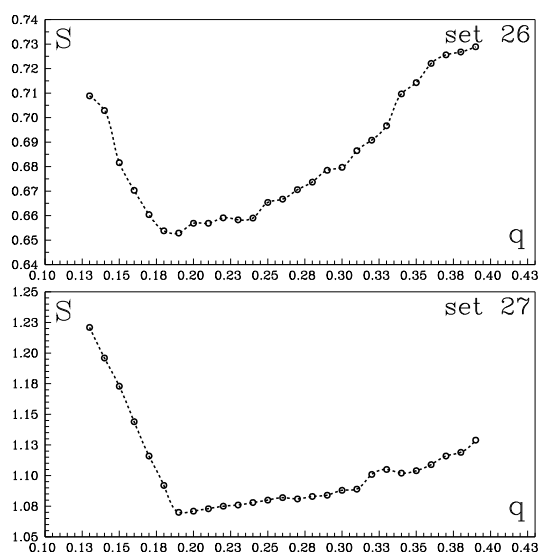


Fig. 4. Parameter $S = \Sigma (O-C)^2$ for the fits done to the light curve of datasets 26 and 27, as a function of mass ratio.

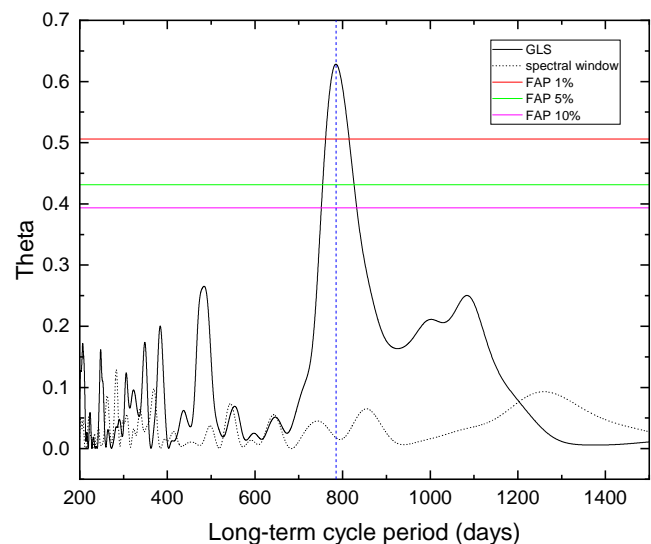


Fig. 5. Generalized Lomb Scargle periodogram for the magnitudes measured at phase 0.25. The vertical line shows the maximum value at 784.8. False alarm probabilities and the spectral window are also shown.

3. Methodology and light curve analysis

In this section we discuss our model for the light curve based only on OGLE data, since the errors associated to MACHO photometry are 10 times larger than those for OGLE data. Therefore, MACHO light curve were used to find additional times of minima only. In order to study the photometric changes, we divided the whole dataset in subsamples of 27 consecutive data sets (Table 2). This allowed us to work with clean orbital light curves with no much influence of the long-term cycle. The choice of a different number of segments does not change the results of this paper. We must keep in mind that the time range must be large enough to include data to represent adequately the orbital light curve, especially eclipses and quadratures, but also short enough to exclude as much as possible the variability due to the long-term cycle.

3.1. The light curve model

Utilizing an advanced simplex algorithm (Dennis & Torczon 1991), the inverse problem was tackled by calibrating the light curve to match the most accurate parameters of the stars-orbit-disk combination for the observed system. The core principles of this model and the procedure for synthesizing light curves are well-documented in the literature (Djurašević 1992, 1996). Further developments and enhancements of this model are also reported (Djurašević, Vince, & Atanacković 2008) and have been successfully applied in the analysis of numerous close binary systems (e.g. Mennickent & Djurašević 2013; Rosales Guzmán et al. 2018; Mennickent et al. 2020b).

The model quantifies the flux from the binary system as the cumulative output of individual stellar fluxes, coupled with the radiation emanating from an optically thick accretion disk encircling the more luminous star. It incorporates the spatial effects induced by the observer's viewing angle. The light contribution from the disk is estimated using localized Planck ra-

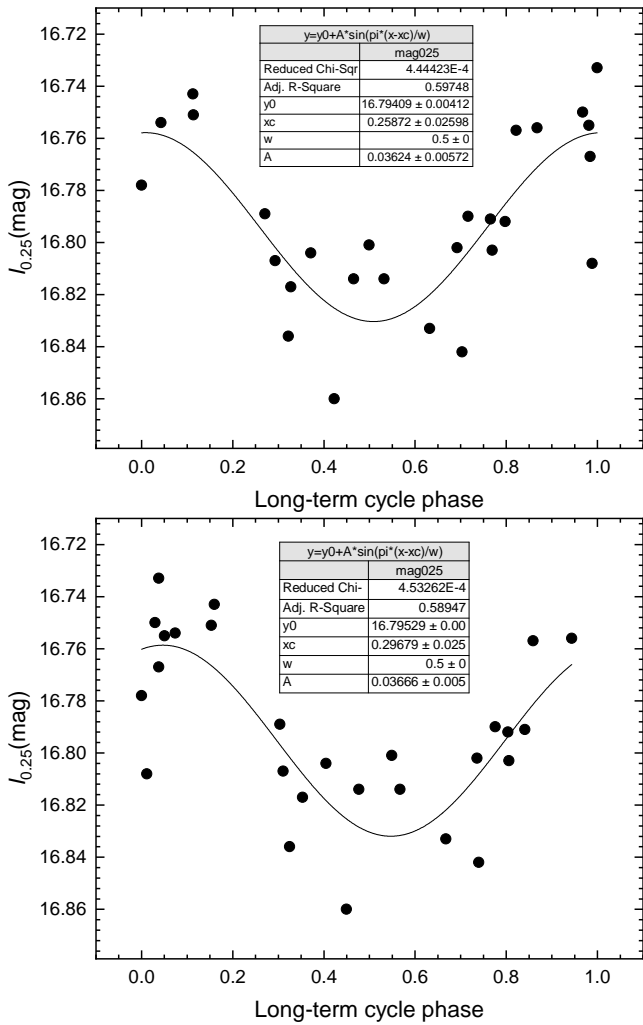


Fig. 6. Magnitudes at phase 0.25 phased with the period of 784^d8 (up) and 778^d8 (down). Phase zero corresponds to HJD' = 2241.7735. Typical error is 0.005 mag. The best sinus fit are also shown.

diation functions at defined temperatures, deliberately omitting the complex calculations involved in radiative transfer. Nevertheless, the model takes into account simpler phenomena like reflection, limb darkening, and gravitational dimming.

The accretion disk is characterized by parameters such as its radius R_d , vertical thickness at its central and outer edges (d_c and d_e , respectively), and a temperature profile that varies with radial distance (e.g. Brož et al. (2021)):

$$T(r) = T_d \left(\frac{R_d}{r} \right)^{a_T}, \quad (3)$$

where T_d signifies the temperature at the disk's outer rim ($r = R_d$) and a_T is the temperature gradient exponent, constrained to $a_T \leq 0.75$. The exponent a_T indicates the degree to which the radial temperature profile approaches a steady-state configuration ($a_T = 0.75$). This ad-hoc radial temperature dependency implies that the disk's surface is warmer closer to the center and gradually cools with increasing radial distance.

Additionally, the model postulates the presence of two shock regions at the disk's periphery: a 'hot spot' near the conjectured impact point where the gas stream from the inner Lagrangian point collides with the disk, and a 'bright spot', located elsewhere along the disk's edge. These regions, characterized by

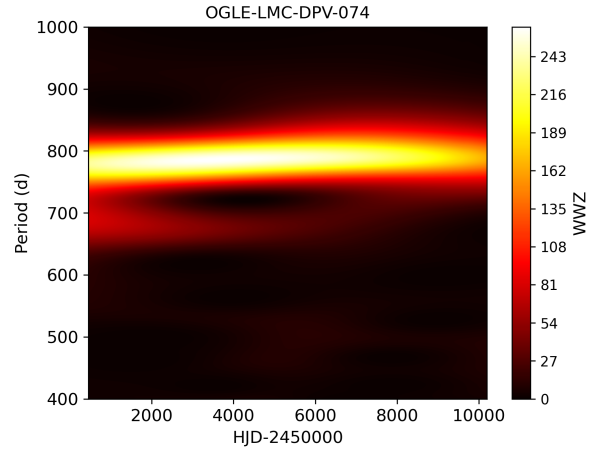


Fig. 7. WWZ transform shows a strong signal around 778.8 days.

variable thickness and temperature compared to the rest of the disk, have been identified in Doppler maps of Algol systems and in hydrodynamic simulations of gas flows in close binary stars (e.g. Albright & Richards 1996; Bisikalo et al. 2000; Atwood-Stone et al. 2012). Their existence was inferred from the analysis of the orbital light curve of the DPV β Lyrae (Mennickent & Djurašević 2013), with interferometric and polarimetric studies further substantiating the presence of the hot spot in this system (Lomax et al. 2012; Mourard et al. 2018). While the genesis of the hot spot is relatively clear, the bright spot's origin could stem from vertical oscillations of gas at the disk's outer edge due to interaction with the incoming matter stream (Kaigorodov, Bisikalo, & Kurbatov 2017). The model's depiction of a singular hot spot on the disk's edge falls short of accurately representing the intricate and variable nature of the light curves, necessitating the inclusion of the bright spot for a more comprehensive description.

In this model, both the hot and bright spots are defined by their relative temperatures $A_{hs} \equiv T_{hs}/T_d$ and $A_{bs} \equiv T_{bs}/T_d$, for their angular dimensions θ_{hs} and θ_{bs} and their angular locations measured from the line joining the stars in the direction of the orbital motion λ_{hs} and λ_{bs} . Additionally, θ_{rad} represents the angle between the line perpendicular to the local disk edge surface and the direction of maximum radiation from the hot spot. The disk radius is also gauged by the parameter $F_d \equiv R_d/R_{yk}$, where R_{yk} is defined as per Djurašević (1992) as the distance from the center of the hotter star to its Roche lobe, measured perpendicular to the line joining the star centers. In this framework, the disk maintains stability only within the boundary $F_d \leq 1$, with any material beyond the Roche limit potentially escaping the system or forming a circumbinary envelope, particularly around the Lagrange equilibrium point L_3 . The stars' gravity-darkening coefficients are set at $\beta_1 = 0.25$ and $\beta_2 = 0.08$, with albedo coefficients $A_1 = 1.0$ and $A_2 = 0.5$, in accordance with von Zeipel's law for radiative shells and complete re-radiation (von Zeipel 1924). The limb-darkening for the components was calculated in the way described by Djurašević et al. (2010).

3.2. Results of the light curve model

In studies of over-contact or semi-detached binaries using photometric time series devoid of spectroscopic data, the "q-search" method is commonly employed to deduce the system's mass

ratio, and it is specially precise for eclipsing systems (Terrell & Wilson 2005). Applying this technique, convergent solutions were obtained for a range of mass ratios $q = M_2/M_1$, where the subscripts "2" and "1" denote the cooler and hotter stars, respectively. We chose datasets 26 and 27 since they accurately represent the orbital light curve with minimum brightness depressions caused by the disk obscuring the primary star. We performed the search in the mass ratio interval 0.13-0.40 with a step of 0.01 and found that a mass ratio of 0.19 aligns pretty well with these datasets (Fig. 4 and Fig. ??). The q error is obtained at the minimum of the S value of the dataset 26. This dataset has a more symmetrical S curve than dataset 27. The 5% S increase from the bottom determines a variation of plus minus 0.01, so we choose a conservative value of ± 0.02 for the mass ratio uncertainty. The q value corroborates earlier findings indicating an average $q = 0.23 \pm 0.05$ (std) in previous studies of DPVs (Mennickent, Otero & Kołaczkowski 2016). In this paper we used $f_g = 84.1$ for the gainer and Ω_1 and Ω_2 equal to 30.702 and 2.208 for the potentials at the gainer and donor surfaces. For that we assumed synchronous rotation of the donor and non-synchronous, critical rotation for the gainer, that fills its critical oval. A second possible model without an accretion disk was not considered, because it leads to an over-contact configuration and requires approximately the same temperatures of the components, which is not in favor of the observations. In addition, the shape of the light-curves for this system is typical for systems with an accretion disk, as well as its changes over time. So far, we have analyzed several similar systems (e.g. Rosales et al. 2023; Mennickent et al. 2022). More reason to reject the model without an accretion disc is our experience with the RY Sct system, which we first modeled within such a model, only to later reject this model based on spectroscopic data and re-analyze the observations within the model with an accretion disc (Djurašević et al. 2001; Djurašević, Vince, & Atanacković 2008).

These datasets were also instrumental in determining the main stellar and orbital parameters. For that, we estimated the mass of the donor star, viz. $1.1 M_\odot$, by assuming a temperature of $T_2 = 5000$ K and applying the corresponding relationships from the Lang tables (Lang 1993) that indicate a spectral type G5 for a luminosity class III star. Utilizing the derived mass ratio, we then calculated the mass of the primary star, that accounts to $5.8 M_\odot$. Additionally, we employed Kepler's third law to determine the orbital separation between the two stars, $90.73 R_\odot$. All derived stellar and orbital parameters, along with their errors, are shown in Table 3. Estimates for the errors of mass, radius, surface gravity and orbital separation are given in the Appendix.

We keep constant these stellar and orbital parameters for other datasets, focusing the analysis on the variability of disk parameters. The outcomes of the light curve modeling are detailed in Table B.2. Uncertainties were estimated with numerical experiments around the best fitting values. They must be observed as generic ones due to the non-homogenous character of the data. Single orbital light curve fittings are presented in Figs. A1-A3, highlighting measurement uncertainties, typical orbital variations, long-term variability, fitting quality, and the system's visual representation. Observed discrepancies exceeding individual data point errors could be attributed to underestimation of formal errors or unaccounted variabilities in the model. For instance, a possible additional light source is not considered. Another possible cause for these discrepancies could be the span of individual light curves over multiple orbital cycles, introducing long-term variability into the analysis. To address this, a "sliding" polynomial of lower degree was fitted through each light curve segment, with magnitudes at orbital phases 0.25

Table 2. Data strings.

set	HJD'-mid	Δt (d)	mag025	mag075	dM/dt	Φ_l
01	2241.7735	148	16.778	16.760	1.77	0.95
02	2494.6013	340	16.836	16.845	1.38	0.27
03	2867.6482	401	16.792	16.790	1.90	0.75
04	3391.7015	641	16.814	16.813	1.46	0.43
05	4041.3132	653	16.807	16.803	2.00	0.26
06	4587.2472	433	16.808	16.780	2.72	0.96
07	4853.1629	95	16.817	16.818	1.43	0.30
08	4928.0578	55	16.860	16.851	1.22	0.40
09	5414.5181	273	16.754	16.734	1.85	0.02
10	5593.4558	118	16.789	16.734	1.43	0.25
11	5672.2730	38	16.804	16.760	1.47	0.35
12	5798.5795	151	16.814	16.820	1.08	0.52
13	5877.0519	58	16.833	16.837	1.40	0.62
14	5932.9618	55	16.842	16.800	3.71	0.69
15	5984.5826	40	16.803	16.763	3.33	0.76
16	6026.0065	59	16.757	16.770	3.04	0.81
17	6165.3956	144	16.733	16.728	2.31	0.99
18	6254.9853	133	16.751	16.728	2.09	0.10
19	6708.9257	310	16.802	16.752	1.00	0.69
20	7038.9236	180	16.743	16.721	1.92	0.11
21	7342.2775	532	16.801	16.770	1.80	0.50
22	7722.7651	148	16.767	16.735	2.08	0.99
23	8297.5512	369	16.790	16.764	2.17	0.73
24	8495.0520	157	16.750	16.730	3.24	0.98
25	9290.3548	1160	16.755	16.725	2.19	0.00
26	9905.8385	77	16.791	16.772	2.90	0.79
27	9985.8180	125	16.756	16.782	2.71	0.89

Note: Mid of the HJD' range, the range of days and the magnitudes at orbital phases 0.25 and 0.75 are given, according to the light curve model. Mass transfer rates, normalized to the value of string 19 and discussed in Section 3.3, are also given, along with the phases of the long-term cycle Φ_l according to Eq. 5.

Table 3. Calculated stellar and orbital parameters.

M_1 (M_\odot)	5.8 ± 0.3	$\log g_1$	4.08 ± 0.04
M_2 (M_\odot)	1.1 ± 0.1	$\log g_2$	1.78 ± 0.03
R_1 (R_\odot)	3.6 ± 0.1	P_o (d)	38.15917 ± 0.00054
R_2 (R_\odot)	22.4 ± 0.8	a_{orb} (R_\odot)	90.7 ± 1.8
T_1 (K)	18701 ± 208	i ($^\circ$)	85.8 ± 0.3
T_2 (K)	5000 ± 200 (fixed)		

Note: We include the orbital separation a_{orb} and the system inclination i . Indexes 1 and 2 refer to hot and cool stellar components. The errors for masses, radius, $\log g$ and orbital separation are those derived in the Appendix, for the other parameters are from light curve fitting.

and 0.75 measured using the corresponding orbital phases and fit values (Table 2).

We find that the disk radius ranges from $31.97 R_\odot$ to $43.81 R_\odot$ whereas the disk temperature ranges from 3258 K to 4217 K. The disk outer vertical thickness span from 6.1 to $12.9 R_\odot$ while the disk height at the inner boundary span from 3.1 to $5.0 R_\odot$. The hot spot temperature is at average 1.28 ± 0.08 times higher than the surrounding disk and the bright spot is 1.14 ± 0.04 times higher than the surrounding disk. The hot and bright spots are located at $327:2 \pm 12:1$ and $94:5 \pm 33:3$, respectively, as measured from the line joining the stars, from the donor to the gainer, and in the sense of the binary motion. The hot and bright spots span arcs of $18:6 \pm 3:1$ and $43:0 \pm 5:5$, respectively, in the disk's outer edge. In general, we do not observe correlations between the fit parameters except for few cases.

3.3. A simple model for the mass transfer rate

We also calculated an approximation for the mass transfer rate \dot{M} , using the following prescription (Mennickent & Djurašević 2021):

$$\frac{\dot{M}_{2,f}}{\dot{M}_{2,i}} = \frac{R_{disk,f}^2 [A_{hs,f} T_{disk,f}]^4 d_{e,f} \theta_{hs,f}}{R_{disk,i}^2 [A_{hs,i} T_{disk,i}]^4 d_{e,i} \theta_{hs,i}}. \quad (4)$$

This equation allows us to estimate relative mass transfer rates at different epochs i and f , for a given system. In order to normalize our determined values of \dot{M} , we used as reference its minimum value, attained at the orbital cycle represented by string 19. These values are shown in Table 2, and an uncertainty of up to 40% is derived from the classical formula of error propagation. The mass transfer rate hence calculated has a mean value of 2.06 with a standard deviation of 0.73, and maximum and minimum values of 3.71 and 1.

3.4. The long-term cycle

In order to investigate the long-term cycle length, we searched for periodicities in the data of magnitudes at phase 0.25 with the aid of the GLS periodogram. We searched between 200 and 1500 days, and find a prominent peak at $784^d \pm 24^d$ (Fig. 5). The magnitudes at phase 0.25 follows a long-term tendency. A sinus fit provides overall I -band amplitude of 0.036 ± 0.006 mag although the peak to peak distance is 0.107 mag (Fig. 6).

The long-term cycle is also revealed in the Weighted Wavelet Z Transform (WWZ) as defined by Foster (1996). The WWZ works in a similar way to the Lomb-Scargle periodogram providing information about the periods of the signal and the time associated to those periods. It is very suitable for the analysis of non-stationary signals and has advantages for the analysis of time-frequency local characteristics. We notice that the WWZ transform for the I -band time series suggests a stable long-term cycle length of 780 days, confirming our finding in the periodogram constructed with magnitudes taken around orbital phase 0.25 (Fig. 7). The period obtained every step of 100 days with the above tool shows a distribution with a mean of $778^d \pm 4^d$ (std). A sinus fit provides overall I -band amplitude of 0.037 ± 0.006 mag and basically the same chi square that the case for the period 784^d (Fig. 6).

In the following, and based on the trial ephemerides shown in Fig. 6, we use as ephemeris for the maximum of the long-term cycle:

$$\text{HJD} = 245\,2280.7 \pm 218.1 + 778^d \pm 4^d \text{E}. \quad (5)$$

Regarding long-term trends, we observe that the disk temperature increases with Heliocentric Julian Date, while the disk radius decreases. Additionally, we find that the disk tends to be hotter when it is smaller (Fig. 8). Throughout the observation period, the mass transfer rate roughly increases (Fig. 9). This observation should be interpreted considering data collected at similar phases of the long-term cycle. It is specially evident in the data colored with blue in the above figure ($\Phi_1 = 0.87\text{-}0.99$). Beyond this overarching trend, the parameter dM/dt also mirrors the long-term cycle, as we will demonstrate next.

We notice that the magnitude at orbital phase of 0.25 mirrors the dynamics of the long-term cycle, similarly to how the mass transfer rate does, as shown in Figure 10. Both parameters

Table 4. Parameters of fits $y = a + bx$ shown in Fig. 8.

Plot	Par.	Value	Std	t-value	Prob > t
T_d -HJD'	a	3227	91	35.3	7.3E-23
T_d -HJD'	b	0.078	0.014	5.43	1.2E-5
R_{disk} -HJD'	a	45.02	1.85	24.4	6.0E-19
R_{disk} -HJD'	b	-0.0011	3E-4	-3.9	6.4E-4
T_d - R_{disk}	a	5524	247	22.4	4.6E-18
T_d - R_{disk}	b	-47.8	6.4	-7.4	8.5E-8

undergo clear changes throughout the long-term cycle, although with significant scatter. Notably, the peak of the long-term cycle nearly aligns with the maximum in the mass transfer rate, and both curves exhibit a slight shift where the mass transfer rate (\dot{M}) precedes the system's brightness. This suggests a causal relationship: an increase in mass transfer rate leads to an increase in system brightness. The enhanced brightness during the peak of the long-term cycle could result from reduced obscuration of the gainer star and a hotter disk, as implied by the d_c and R_{disk} diagrams in Fig. 11. In the same figure we observe that the hot spot position moves closer to the line joining the stars around $\Phi_l = 0.3$.

Interestingly, the long-term tendency of disk radius can be observed in the polar diagram of Fig. 12. We see that larger disk are found at the earliest epochs, whereas smaller disk can be found at later epochs. It is at earlier epochs when the bright spot attains larger extension and it is distributed over a wider area in the outer disk.

4. On the evolutionary stage

We use the Modules for Experiments in Stellar Astrophysics (MESA), a powerful and widely used suite of open-source computational tools designed for astrophysical research (Paxton et al. 2011, 2015). In particular, when studying binary star evolution, MESA is extremely useful due to its robust and detailed simulations of stellar physics. Crucial for binary star evolution, MESA can simulate interactions between the stars, such as mass transfer, common envelope phases, and tidal effects. These interactions significantly influence the evolution and fate of binary systems. For our purposes, we customize MESA following Rosales et al. (2024), matching the scenario of mass transfer by Roche lobe overflow between two intermediate mass stars.

We performed several trials with initial stellar masses in a range $3.4\text{--}5.8 M_\odot$ for the donor and $1.0\text{--}3.4 M_\odot$ for the gainer, both with step of $0.05 M_\odot$ and orbital periods in a range $1\text{--}10$ days with step 1.0 day, allowing the systems to evolve from its initial condition. We fixed the metallicity to $Z = 0.006$, roughly representative for the Large Magellanic Cloud (Eggenberger et al. 2021). We constructed models that were compared with the observed system properties. Among these models we selected those that minimized the χ^2 parameter, representing mean deviations of the system parameters regarding those of theoretically calculated values. Following Rosales et al. (2024), the prescription for mass transfer considered the fraction of mass lost from the vicinity of donor as fast wind as $1\text{E-}3$, the fraction of mass lost from the vicinity of accretor as fast wind as $1\text{E-}4$ and no mass lost from a possible circumbinary matter. The first two parameters were allowed to vary from $1\text{E-}1$ to $1\text{E-}12$ in steps of 1 dex. These values were chosen as representative of a case with very small or neglectable mass loss, considering that the more evolved donor should have a wind larger than the B-type dwarf. In other words, we considered quasi-conservative models. The

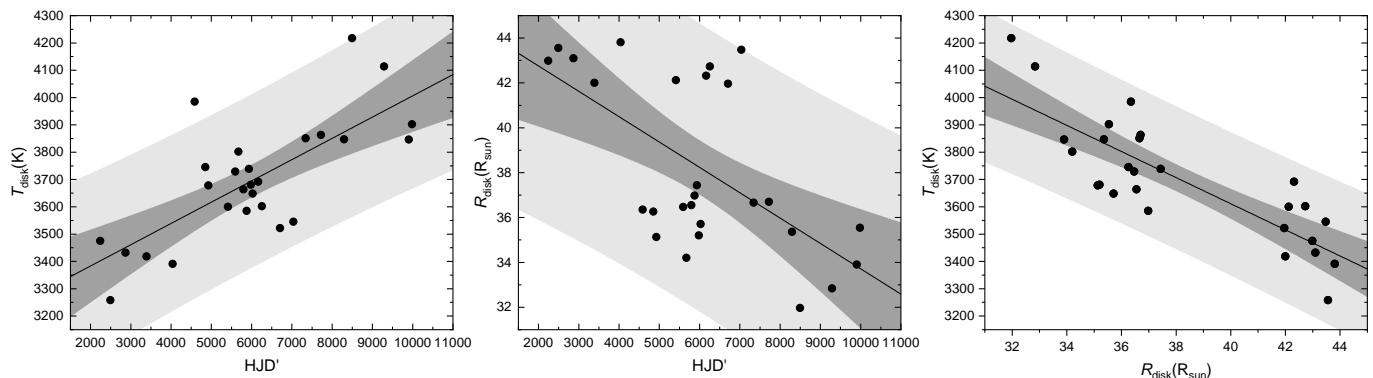


Fig. 8. Behaviour of some disk parameters according to our models. Typical errors are 60 K and $0.1R_{\odot}$. Best linear fits are shown along with grey light and grey dark regions indicating 95% prediction and confidence bands, respectively. Parameters for these fits are given in Table 4.

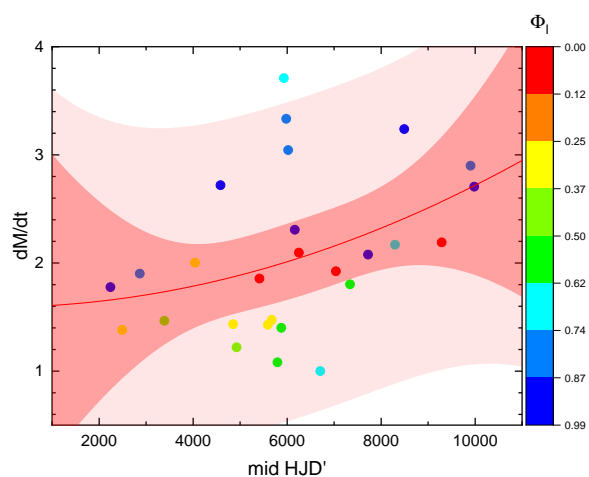


Fig. 9. Mass transfer rate versus the mid HJD' given in Table 2 with colors indicating ranges of the long-term cycle phase. The best quadratic fit, $y = (1.59055) + (5.948E-6) * x + (1.06792E-8) * x^2$ is shown, along with grey light and grey colored regions indicating 95% prediction and confidence bands, respectively.

mixing length parameters for donor and gainer were allowed to vary from 0.3 to 1.9 in steps of 0.1 and the final values chosen were 1.0 both. The parameter for semi convection was fixed to 0.01. The above values guarantee an effective convective mixing of chemical species. In order to explore magnetism in the donor star, we activate rotation in the MESA code, enabling also thermo-haline mixing. On the contrary, in order to keep simple and fast the calculations, we assumed zero rotation for the gainer switching off this mode.

Our studies showed that the present day binary parameters can be reproduced by a binary of initial period 7 days and initial masses 3.5 and 3.3 M_{\odot} and current age 200.54 Myr. The evolution of the best model is summarized in Table 5, at specific evolutionary stages labeled accordingly, and from the Zero Age Main Sequence to ${}^4\text{He}$ depletion.

The stellar and system parameters found compare well with those reported in Table 3; namely, theoretical masses 5.6 and 1.2 M_{\odot} versus 5.8 and 1.1 M_{\odot} calculated radii of 23.0 and 3.8 R_{\odot} versus 22.4 and 3.6 R_{\odot} and orbital period $38^{\text{d}}16$ versus $38^{\text{d}}16$. Regarding the luminosities, the theoretical temperatures are $\log T = 3.72$ and 4.29 K, versus $\log T = 3.70$ and 4.27 K. We notice a small discrepancy with the luminosity of the gainer, and this principally produces the mismatch between the observed data and the predicted position (X_2 stage) in Fig.

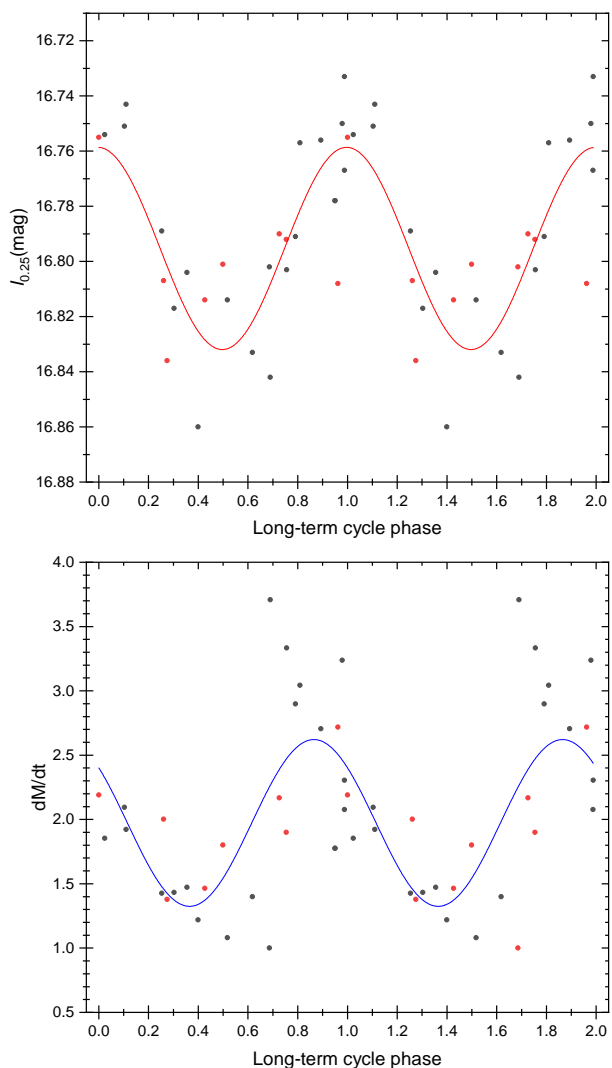


Fig. 10. \dot{M} and I -band magnitude, measured at orbital phase 0.25, as a function of the long-term cycle phase, based on the analysis of the light curve strings of Table 2. Red (black) dots correspond to data of datasets whose time span is longer (shorter) than 35% of the cycle length. Best sinus fits are also shown.

13. This is observed even at trials with metallicities of $Z = 0.02$ and 0.003. It can, in principle, be attributed to the presence of the disk, that hides the more massive star and whose influence in the flux balance has not been included in the MESA calculations. For

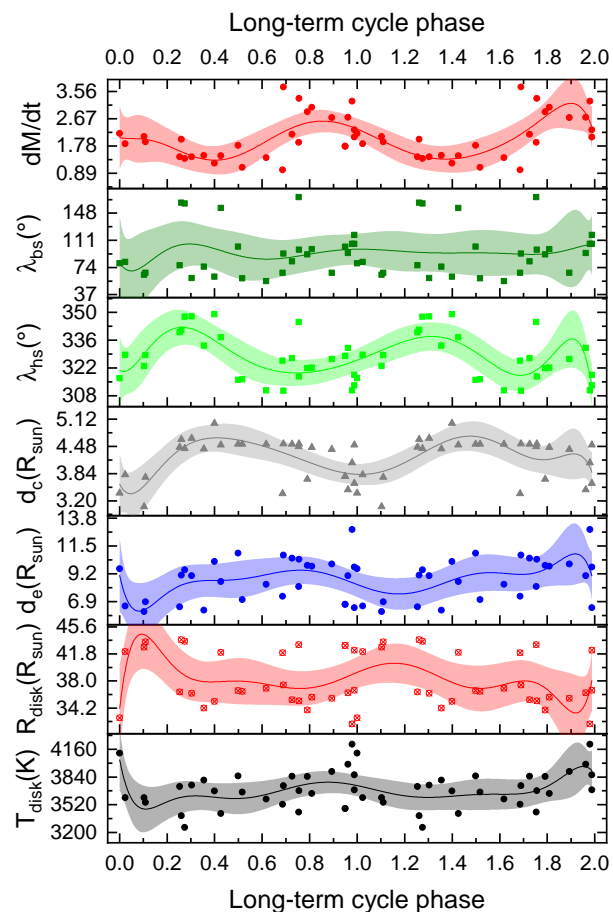


Fig. 11. Behaviour of some disk parameters during the long-term cycle. Polynomial fits of degree 9th are shown to illustrate tendencies.

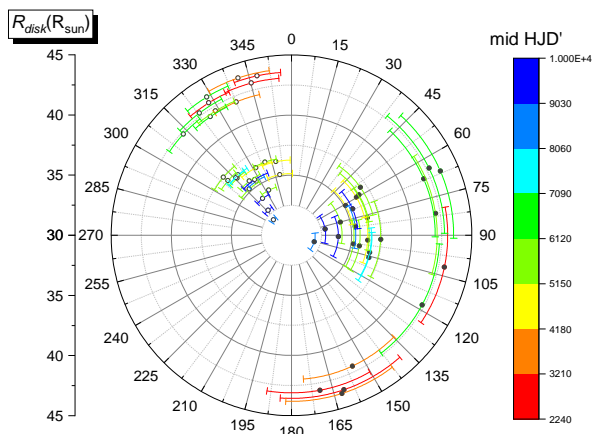


Fig. 12. Radial position and angular extension of hot spot (open circles) and bright spot (dots) at different epochs.

the same reason, we observe our simulations as general insight of the possible evolutionary path for the binary, and we do not pursue a better approximation, although it is remarkable that the best model is in fact found in a mass transfer stage, with $dM/dt = 3.5 \times 10^{-6} M_{\odot}/\text{yr}$. The donor is found after hydrogen depletion and with important helium enhancement in its core, while the gainer has rejuvenated acquiring $2.3 M_{\odot}$ during the accretion process (Table 5 and Fig. 14). The system already passed by the optically thick mass transfer stage and now it is in a milder stage of mass transfer. During the binary evolution, the donor in-

creased its radius from $2.2 R_{\odot}$ to $23 R_{\odot}$ and the orbital period increased from 7^{d} to the current value of $38^{\text{d}}16$. The Hertzsprung-Russell (HR) diagrams show the huge decrease of temperature of the donor star, and the increase of luminosity of the gainer, until reaching the current stage. They also show an expected decrease of the hydrogen and the increase of the helium fraction in the core of the gainer and the donor (Fig. 14). Furthermore, our MESA simulations shows, as expected, how the temperature of the donor evolves first at a nuclear timescale and then, after filling the Roche lobe, at a much shorter thermal time scale when mass transfer occurs. The same for the donor radius, that slightly increases during millions of years to change abruptly, after starting the mass transfer process (Fig. 15).

We find the system in a mass transfer stage, returning from a huge burst of mass transferred to the gainer at maximum rate of $1 \times 10^{-4} M_{\odot}/\text{yr}$; at present time the rate of mass transfer has slowed to $dM/dt = 3.46 \times 10^{-6} M_{\odot}/\text{yr}$. The overall process, from stages E to H, will last about 655 000 years (Fig. 16).

We further analyze the internal structure of both the donor and the gainer stars using Kippenhahn diagrams (Fig. 17). For the case of the donor, which starts from the ZAMS (Zero Age Main Sequence) until helium depletion $X(\text{He}_c) < 0.2$, we were able to identify that the convective zone of the donor star is below $0.5 M_{\odot}$ while mostly all nuclear production occurs below $1 M_{\odot}$. Additionally, both zones of convection and nuclear production gradually decrease as the system evolves and approaches mass transfer as expected (E stage). Zones of thermohaline instability activation intermittently appear at different stages of evolution. In addition, the overshooting zone is present only until mass transfer occurs and then disappears once mass transfer begin.

For the gainer star, we identified a convective zone from its center to $0.5 M_{\odot}$ with a nuclear production rate zone that remains largely unchanged for most of its lifetime from the ZAMS (Zero Age Main Sequence) to moments prior to mass transfer (E-stage). In addition, we identified an overshooting zone from 0.7 to $0.9 M_{\odot}$. However, after mass transfer, its convective core immediately grew twice the original size, in terms of total mass. Following this, the overshooting zone appears between 1.5 and $2.0 M_{\odot}$. Additionally, the nuclear production zone increased significantly, occurring within a central mass of $3 M_{\odot}$ after mass transfer.

We calculated the magnetic field structure due to the Taylor-Spruit (ST) dynamo, in particular the toroidal and poloidal components, that resulted of the order of few Gauss in the stellar subsurface. On the other hand, the Eulerian diffusion for mixing and the Spruit-Taylor diffusion coefficient and the angular velocity were also calculated and are shown in Fig. 18. The magnetic fields obtained with the ST prescription, of the order of few Gauss, are too weak to be detected observationally with the current usual instrumentation.

5. Discussion

Before we proceed with the interpretation of our results, it's important to be aware of the limitations of our model. A key simplification is our focus exclusively on circumstellar material within the disk, thereby overlooking any light contributions originating from regions above or below the disk plane. Additionally, we have assumed the gainer is surrounded by an accretion disk, disregarding other potential light sources such as jets, winds, and outflows. Nonetheless, the model allows for the possibility of accounting for variations in disk emissivity that are dependent on azimuthal position through the inclusion of two disk spots. Despite these constraints, and drawing on prior research on algols

Table 5. Evolutionary stages of OGLE-LMC-ECL-14413.

	Stage	Age (Myr)	M (M_{\odot})	R (R_{\odot})	P _o (d)	log T (K)	\dot{M} (M_{\odot} yr ⁻¹)	Ev. process
Donor	A	0.0000	3.5000	2.1860	7.0000	4.2122	-1.807E-12	Zero Age Main Sequence (ZAMS)
	B	39.2148	3.4999	2.1619	7.0005	4.1848	-3.953E-12	Terminal Age Main Sequences (TAMS)
	X ₁	100.0000	3.4995	2.6076	7.0014	4.1694	-6.338E-12	Inversion ¹ H/ ⁴ He donor
	C	195.2898	3.4983	5.9322	7.0050	4.0558	-7.298E-11	Depletion of central hydrogen ¹ H
	D	200.2644	3.4979	5.1146	7.0059	4.1145	-3.715E-11	Size increase beyond the RL due to depletion of ¹ H
	E	200.4263	3.4979	11.0219	7.0060	3.9503	-7.255E-10	Initiation of mass transfer
	U ₁	200.4512	3.3590	11.2709	6.9961	3.8998	-1.351E-05	Mass inversion (M ₁ = M ₂)
	F	200.4700	2.9999	10.9856	7.2961	3.8076	-2.406E-05	Minimum value Roche Lobe
	G	200.5200	1.5973	16.0870	18.8282	3.6227	-3.900E-05	Maximum mass transfer
	U ₂	200.5333	1.2091	21.9994	34.9631	3.6890	-1.004E-05	End of optically thick mass transfer
Gainer	a	0.0000	3.3000	2.1194	7.0000	4.1981	-1.049E-12	Zero Age Main Sequence (ZAMS)
	b	39.2148	3.2999	2.0593	7.0005	4.1706	-2.449E-12	Terminal Age Main Sequences (TAMS)
	c	200.4263	3.2992	4.0710	7.0060	4.0943	-8.432E-12	Initiation of mass accretion
	U ₁	200.4512	3.4379	4.664	6.9961	4.1410	1.349E-05	Mass inversion (M ₁ = M ₂)
	d	200.5200	5.1976	4.6279	18.8282	4.2924	3.895E-05	Maximum mass accretion and relocation to HR diagram
	U ₂	200.5333	5.5854	4.0368	34.9631	4.3001	1.003E-05	End of optically thick mass accretion
	X ₂	200.5408	5.6294	3.7647	38.1664	4.2946	3.451E-06	Current stage
	H	201.0810	0.80231	36.5068	94.9661	3.7982	-7.685E-08	end mass transfer
	I	210.5306	0.7926	0.24643	95.3674	4.6073	-3.059E-10	⁴ He depletion

Note: Evolutionary stages of OGLE-LMC-ECL-14413, from Zero Age Main Sequence (ZAMS) to ⁴He depletion of the donor star, according to the best model. Detailed descriptions of key features are provided, along with corresponding ages measured in Mega years (Myr).

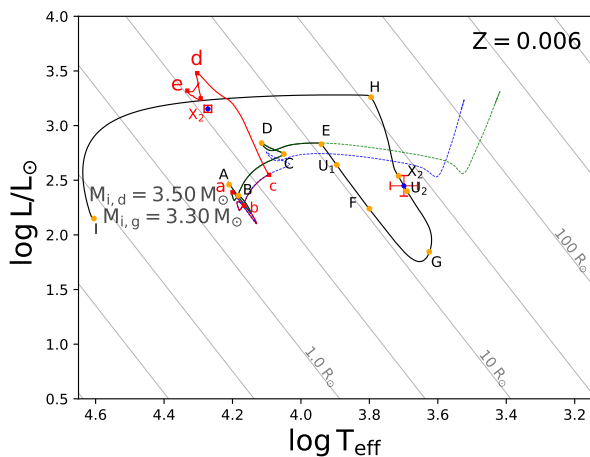


Fig. 13. Evolutionary paths of the donor and the gainer for the best model. Model initial and best-fit mass values are shown, along with letters indicating the evolutionary stages described in Table 5.

with disks, our model likely captures the principal light sources for the continuum light. This is evidenced by the close correspondence between the model light curve and the orbital and long-term light curves over the span of 21.7 years of observation (the time covered by the *I*-band OGLE time series). In addition, we run evolutionary models and find the best one reproducing the present state of the system. Although the match is not perfect, we can certainly infer that the system is product of the evolution of a stellar pair that experienced strong mass transfer in the past, or is still in a semidetached stage with Roche lobe overflowing.

The fractional radius of the gainer is $R_1/a = 0.04$. This value reveals that there is enough room around the gainer for the formation of an accretion disk, since for the system mass ratio, the accreting star is smaller than the circularization radius, where a particle released at the inner Lagrangian point arrives to conserve

its angular momentum (Lubow & Shu 1975). The low value of the fractional radius is due to the large orbital separation and long orbital period of this system and it is consistent with the existence of an accretion disk inferred from the light curve model. It is comparable to the value obtained for the long period system V495 Cen (Rosales Guzmán et al. 2018; Rosales et al. 2021). Interestingly, in OGLE-LMC-ECL-14413, the disk vertical height near the star is larger than twice the gainer radius, provoking a significant occultation of the star.

During the 30.85 year time baseline the system shows systematic changes of disk properties, in particular its vertical height at the outer edge. In hydrostatic equilibrium, the vertical height H of an accretion disk at radius R_d is:

$$\frac{H}{R_d} \approx \frac{c_s}{v_k} = c_s \sqrt{\frac{R_d}{GM_1}}, \quad (6)$$

where v_k is the Keplerian velocity and c_s the sound speed, that for an isothermal perfect gas can be approximated as:

$$c_s \approx 10 \sqrt{\frac{T}{10^4 K}} \text{ km s}^{-1}, \quad (7)$$

(Eqs. 3.35 and 3.32 in Kolb 2010). Using the mean parameters at the outer and inner disk we get $(v_k, c_s) = (164, 6.1)$ and $(552, 13.7)$ in km s^{-1} , respectively, yielding $H/R = 0.04$ and 0.02 . Considering the averages $d_e/R_d = 0.23$ and $d_c/R_1 = 1.15$ and that the vertical thickness is twice H , we conclude that the disk vertical height is larger than expected for hydrodynamical equilibrium, at the inner and outer boundaries, suggesting that turbulent motions dominate the disk vertical structure. In this context, it may be worth mentioning that in a detailed model of β Lyrae, the disk height had to be multiplied by a factor about 4 times its expected equilibrium value, possibly reflecting non-negligible hydrodynamic flows within the disk (Brož et al. 2021). These turbulent

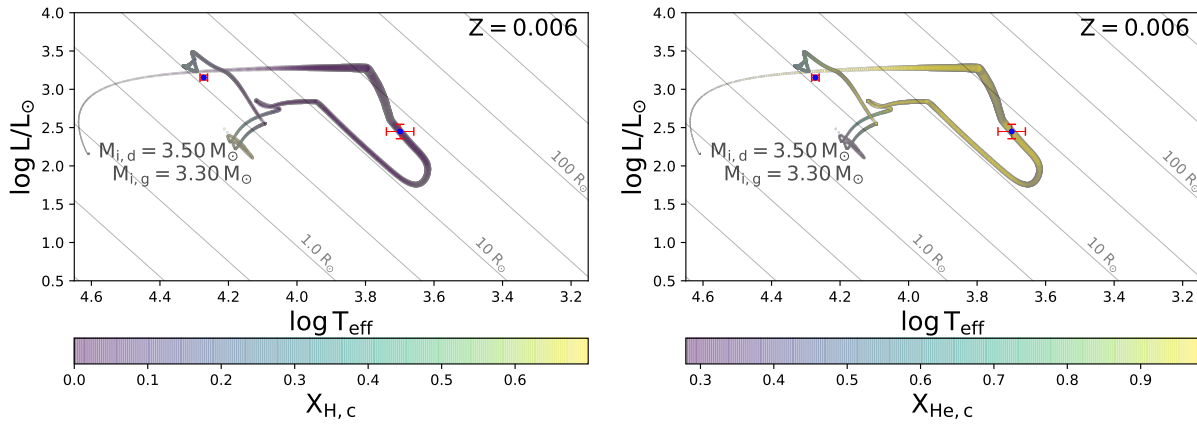


Fig. 14. HR diagrams indicating the system evolution along with the hydrogen and helium fractions in the stellar cores.

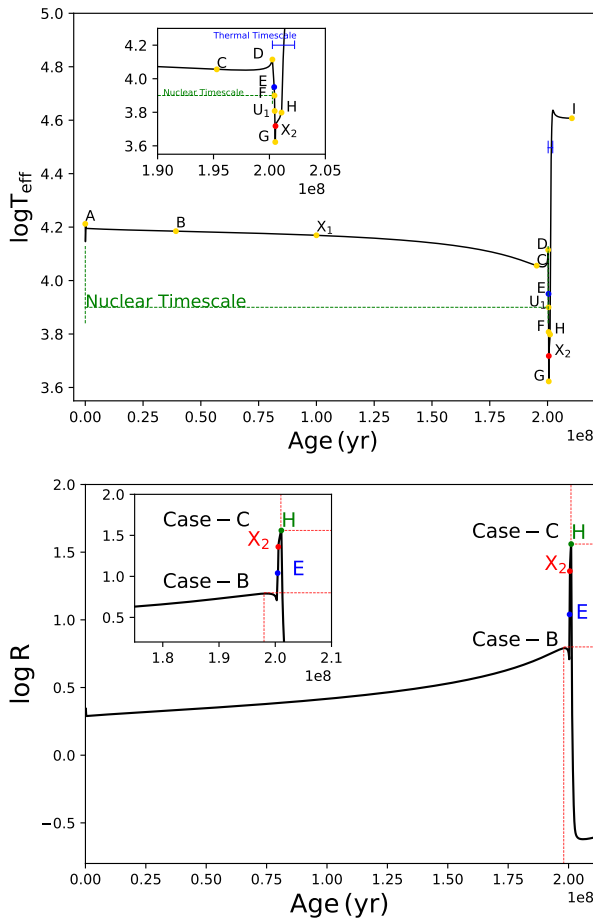


Fig. 15. (Left) Evolution of the donor star size with an initial mass of $3.5 M_{\odot}$ in the binary system OGLE-LMC-ECL-14413, with a companion that has an initial mass of $3.3 M_{\odot}$, showing the phases in which cases A, B, and C of RLOF can occur, depending on the age of the system. The inversion of the $^1\text{H}/^4\text{He}$ ratio (X_1 stage) is represented by a yellow dot, the mass transfer (E stage) by a blue dot, and the current stage of the system (X_2 stage) by a red dot. (Right) Effective temperature T_{eff} as function of age for OGLE-LMC-ECL-14413. We show that the donor star, after crossing the Hertzsprung gap during the onset of the blue loop (Stages C and D), follows an evolutionary track until reaching its current stage (X_2 stage) on a thermal timescale. This continues until reaching the final stage of non optically-thick mass transfer (H-stage), stopping shortly before Helium depletion.

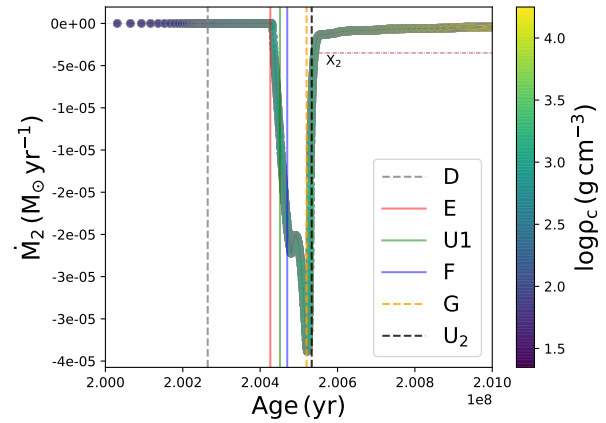


Fig. 16. Mass transfer rate versus the system's age for the best model. Vertical lines indicate the evolutionary stages described in Table 5. The density in the core of the donor star is also shown.

motions could be produced by the continuous injection of mass from the inner Lagrangian point, through a gas stream, into the accretion disk. Incidentally, the variable thick disk explains why the primary and secondary eclipses relative depth reverses, since part of the gainer is hidden by the disk that masks its luminosity to a variable degree. In addition, the variable projected disk area into the visual line of sight contributes to occult a fraction of the donor while it is eclipsed. The low contribution of the gainer to the total flux is reproduced by our models as shown in Figs. A1-A3.

In principle, the disk can be stable until the last non-intersecting orbit defined by the tidal radius (Paczynski 1977; Warner 1995, Eq. 2.61):

$$\frac{R_t}{a_{\text{orb}}} = \frac{0.6}{1+q}, \quad (8)$$

we get $R_t/a_{\text{orb}} = 0.50$, or $R_t = 45.4 R_{\odot}$. We observe that during all the observing epochs the disk outer radius keeps inside the volume defined by the tidal radius.

The value of the mass transfer rate found $3.5 \times 10^{-6} M_{\odot}/\text{yr}$, must be consensual with the constancy of the orbital period. For a binary system ongoing conservative mass transfer, we should expect a change of the orbital period of (Huang 1963):

$$\frac{\dot{P}_0}{P_0} = 3\dot{M}_2 \left(\frac{1}{M_2} - \frac{1}{M_1} \right) = 7.6 \times 10^{-6} \text{yr}^{-1} \quad (9)$$

This means a change of 2.9×10^{-4} days per year, or 8.9×10^{-3} days during the whole observing window. This is not observed, therefore the actual mass transfer rate is smaller than $3.5 \times 10^{-6} M_\odot/\text{yr}$ or systemic mass loss is important for the angular momentum balance.

As previously said, a magnetic dynamo in the donor has been invoked as the origin of the long-term cycle. The idea behind this scenario is that the dynamo produces cyclic changes in the equatorial radius of the donor star, enhancing quasi-periodically the amount of mass transferred onto the gainer. This should produce effects in the accretion disk, that is exposed to cycles of enhanced mass transfer. These effects could be changes in the disk radius, height or even disk temperature. An insight favoring the dynamo hypothesis is the discovery that the donor dynamo number increases during epochs of high mass transfer in DPVs (Mennickent, Schleicher, & San Martín-Pérez 2018; San Martín-Pérez et al. 2019). In addition, the calculated long period for OGLE-LMC-ECL-14413, according to the formula given by Schleicher & Mennickent (2017), is 820 days, close to the values obtained from the periodograms and the WWZ analysis. However, our MESA analysis shows that the magnetic fields, at least those calculated from the Spruit-Taylor prescription, are usually less than a thousand of Gauss, i.e. too low to produce observable effects, as we will show now.

It has been shown that fluctuations in the radius of a star can be attributed to the gravitational interaction between the orbit and changes in the configuration of a magnetically active star within the binary system. As the star progresses through its activity cycle, variations in the distribution of angular momentum lead to the star's changing shape. Variations in the overfill factor of the Roche lobe should produce changes in mass transfer rate. This was proposed as a possible origin for the DPV long-term cycles by Schleicher & Mennickent (2017). The change in the stellar radius $\Delta R = R_{new} - R$, derived from the prescription of Applegate (1992, eqs. 7 and 23) is given by:

$$\frac{\Delta R}{R} = \frac{2}{3} \frac{R^4}{GM^2} B^2 \quad (10)$$

where B is the subsurface magnetic field strength. On the other hand, the expected mass transfer rate is given by (Ritter 1988):

$$\dot{M} = \dot{M}_0 e^{\frac{\Delta R}{H_2}} \quad (11)$$

where \dot{M}_0 is the mass transfer rate when $B = 0$, and it can be assumed as constant, whereas H_2 is the pressure scale height in the Roche potential given by:

$$H_2 = \frac{kT\mu}{m_p g} \quad (12)$$

where k is the Boltzmann constant, T the donor temperature, m_p the proton mass, g the local acceleration of gravity, and μ is the mean molecular weight, assumed 1.23 for a star in the LMC with $Z \approx 0.01$. In addition, from equations 8 and 9 we get:

$$\dot{M} = \dot{M}_0 e^{\frac{2}{3} \frac{R^5}{H_2 GM^2} B^2} \quad (13)$$

Considering values of $R = 22.42 R_\odot$, $M = 1.1 M_\odot$ and $T = 5000$ K we get $H_2 = 56\,284\,560$ m, i.e. $R/H_2 = 277.4$. If we furthermore consider a subsurface magnetic field strength of 10kG, we get a fractional radius change $\Delta R/R$ of order of $7.3E-6$ and a change in mass transfer rate by a factor $\exp(2.06E-3)$, i.e. negligible. Therefore, we need larger magnetic field strengths than those produced by the Spruit-Taylor mechanism in the donor subsurface to produce appreciable changes in mass transfer rates and in particular, to reproduce the broad range of values shown in Table 2. New investigations of the 3D internal magnetic structure and its dependence on rapid rotation and its temporal evolution should be important to shed light on the importance of stellar magnetism for the DPV long-term cycles, possibly following the techniques and methodologies developed by Navarrete et al. (2023).

6. Conclusion

We have investigated the intriguing light curve of the Double Periodic Variable OGLE-LMC-ECL-14413, spanning 30.85 years. Our model successfully reproduces the overall I -band light curve, capturing both the orbital variability with a periodicity of $38^d.16$ and the DPV cycle, which has a duration of approximately 780 days and exhibits a full amplitude of $0^m.076$ at the I -band. This model includes the light contribution from an accretion disk, characterized by an average radius of $38 R_\odot$, and two hot shock regions located at the outer disk edge. Additionally, for the first time, we have measured fundamental stellar parameters for this system. Our findings include stellar components with masses of 5.8 ± 0.3 and $1.1 \pm 0.1 M_\odot$, radii of 3.6 ± 0.1 and $22.4 \pm 0.8 R_\odot$, and temperatures of 18701 ± 208 K and 5000 ± 200 K, respectively. These stars are separated by a distance of $90.7 \pm 1.8 R_\odot$, and exhibit surface gravities ($\log g$) of 4.08 ± 0.04 and 1.78 ± 0.03 .

Our findings trace the evolutionary history of the system, revealing that it is currently experiencing a burst of mass transfer as the donor fills its Roche lobe. We also observe significant changes in the disk's vertical height, suggesting that turbulent motions contribute to the disk's vertical extension. The system comprises a B-type dwarf, approximately spectral type B3, accreting matter from a cooler, K5-type giant star, according to the spectral classification scheme given by Harmanec (1988). Our MESA simulations, employing the Spruit-Taylor prescription for magnetism, indicate only weak magnetic fields on the cooler star's subsurface, insufficient to account for the observed changes in mass transfer rate.

In terms of the broader context of Double Periodic Variables, our work aligns with previous studies such as those of OGLE-LMC-DPV-097 and OGLE-BLG-ECL-157529 (Garcés et al. 2018; Mennickent & Djurašević 2021), which have also noted long-term changes in accretion disk properties that influence the orbital light curve's shape. Specifically, the maximum brightness during the long-term cycle in both OGLE-BLG-ECL-157529 and OGLE-LMC-ECL-14413 can be attributed to less obscuration of the gainer by a thinner, hotter disk, thereby increasing the visible surface of the gainer. For OGLE-LMC-ECL-14413, the most significant finding is that the long-term cycle could be driven by changes in mass transfer rate, as illustrated in Fig. 10, and that the peak of the long-term cycle occurs when the disk is hotter and thinner.

The DPV phenomenon is both fascinating and inherently complex. Future investigations involving high spectral resolution data and decade-long time series are poised to illuminate this phenomenon further. Moreover, new theoretical simulations

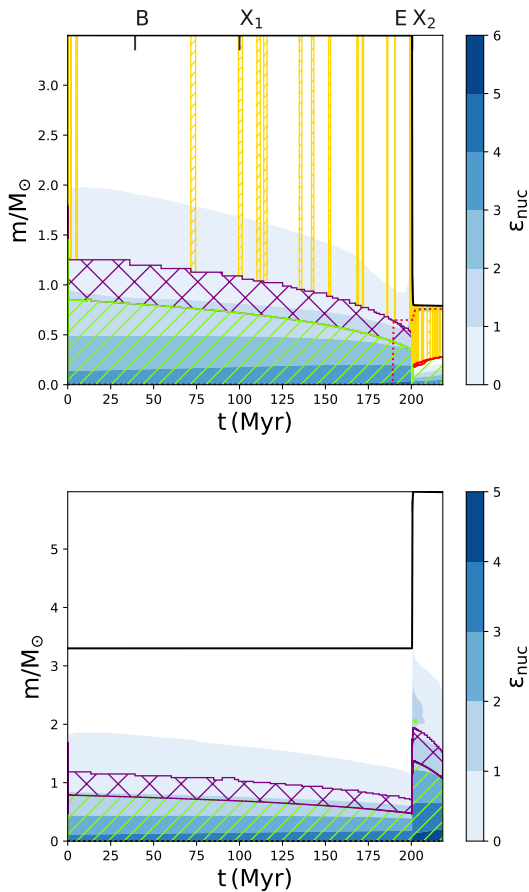


Fig. 17. Kippenhahn diagrams showing the internal structure of the donor (up) and gainer (down) stars. Diagrams with initial masses 3.5 and $3.3 M_{\odot}$ are shown. The evolutionary calculations were stopped when the donor star reached core helium depletion $X(\text{He}_c) < 0.2$. The x-axis gives the age after ignition of hydrogen in units of Myr. The different layers are characterized by their values of M/M_{\odot} . The convection mixing region is represented by hatched green, semi convection mixing region in red and the overshooting mixing region in crosshatched purple. The red dots represent the He core mass while the thermohaline mixing region is represented in hatched yellow. The solid black lines show the surfaces of the stars.

that leverage increased computational power will enhance our understanding of these binary systems.

7. Data availability

Figs. A1-A3 are available at:
<https://doi.org/10.5281/zenodo.14192345>

Acknowledgements. We thank an anonymous referee for the useful comments and suggestions on the first version of this manuscript. We acknowledge support by the ANID BASAL project Centro de Astrofísica y Tecnologías Afines ACE210002 (CATA). This research has made use of the SIMBAD database, operated at CDS, Strasbourg, France. This work has been co-funded by the National Science Centre, Poland, grant No. 2022/45/B/ST9/00243.

References

Albright G. E., Richards M. T., 1996, *ApJ*, 459, L99.
 Applegate J. H., 1992, *ApJ*, 385, 621.

- Atwood-Stone C., Miller B. P., Richards M. T., Budaj J., Peters G. J., 2012, *ApJ*, 760, 134.
 Bisikalo D. V., Harmanec P., Boyarchuk A. A., Kuznetsov O. A., Hadrava P., 2000, *A&A*, 353, 1009.
 Brož M., Mourard D., Budaj J., et al., 2021, *A&A*, 645, A51.
 Dennis, J.E., Torczon, V., 1991, Direct search methods on parallel machines, in *SIAM Journal on Optimization*, Vol.1, Issue 4, pages 448-474
 Djurašević G., 1992, *Ap&SS*, 196, 267.
 Djurašević, G. 1996, *Ap&SS*, 240, 317.
 Djurašević G., Zakirov M., Eshankulova M., Erkapic S., 2001, *A&A*, 374, 638.
 Djurašević G., Vince I., Atanacković O., 2008, *AJ*, 136, 767.
 Djurašević G., Latković O., Vince I., Cséki A., 2010, *MNRAS*, 409, 329.
 Eggenberger P., Ekström S., Georgy C., Martinet S., Pezzotti C., Nandal D., Meynet G., et al., 2021, *A&A*, 652, A137.
 Eggleton P., *Evolutionary Processes in Binary and Multiple Stars*, by Peter Eggleton, Cambridge, UK: Cambridge University Press, 2011.
 Foster G., 1996, *AJ*, 112, 1709.
 Gaposchkin S., 1944, *ApJ*, 100, 230.
 Garcés L. J., Mennickent, R. E., Djurašević, G., Poleski, R., Soszyński, I. 2018, *MNRAS*, 477, 11.
 Graczyk D., Soszyński I., Poleski R., Pietrzyński G., Udalski A., Szymański M. K., Kubiak M., et al., 2011, *AcA*, 61, 103.
 Guinan E. F., 1989, *SSRv*, 50, 35.
 Harmanec P., 1988, *Bulletin of the Astronomical Institute of Czechoslovakia*, 39, 329.
 Hill G., Harmanec P., Pavlovski K., Bozic H., Hadrava P., Koubsky P., Ziznovsky J., 1997, *A&A*, 324, 965.
 Huang S.-S., 1963, *ApJ*, 138, 471.
 Joshi Y. C., Panchal A., 2019, *A&A*, 628, A51.
 Kaigorodov P. V., Bisikalo D. V., Kurbatov E. P., 2017, *Astronomy Reports*, 61, 639.
 Kolb U., 2010, *Extreme Environment Astrophysics*, Cambridge University Press, ISBN: 9780521187855.
 Koubsky P., Harmanec P., Bozic H., Rercy J. R., Ziznovsky J., Huang L., Richards M. T., et al., 1998, *Hvar Observatory Bulletin*, 22, 17.
 Lang, K., 1993, *Astronomy*, vol. 21, no. 2, p. 95.
 Lomax J. R., Hoffman J. L., Elias N. M., Bastien F. A., Holenstein B. D., 2012, *ApJ*, 750, 59.
 Lorenzi L., 1980, *A&A*, 85, 342.
 Lubow S. H., Shu F. H., 1975, *ApJ*, 198, 383.
 Mennickent, R. E., 2017, *Serbian Astronomical Journal*, 194, 1.
 Mennickent, R. E., Pietrzyński, G., Diaz, M., Gieren, W., 2003, *A&A*, 399, 47.
 Mennickent R. E., Djurašević G., 2021, *A&A*, 653, A89.
 Mennickent R. E., Djurašević G., 2013, *MNRAS*, 432, 799.
 Mennickent, R. E., Otero, S., Kołaczowski, Z. 2016, *MNRAS*, 455, 1728.
 Mennickent R. E., Schleicher D. R. G., San Martín-Pérez R., 2018, *PASP*, 130
 Mennickent R. E., Cabezas M., Djurašević, G., Rivinius T., Hadrava P., Poleski R., et al., 2019, *MNRAS*, 487, 4169.
 Mennickent R. E., Garcés J., Djurašević, G., et al., 2020a, *A&A*, 641, A91.

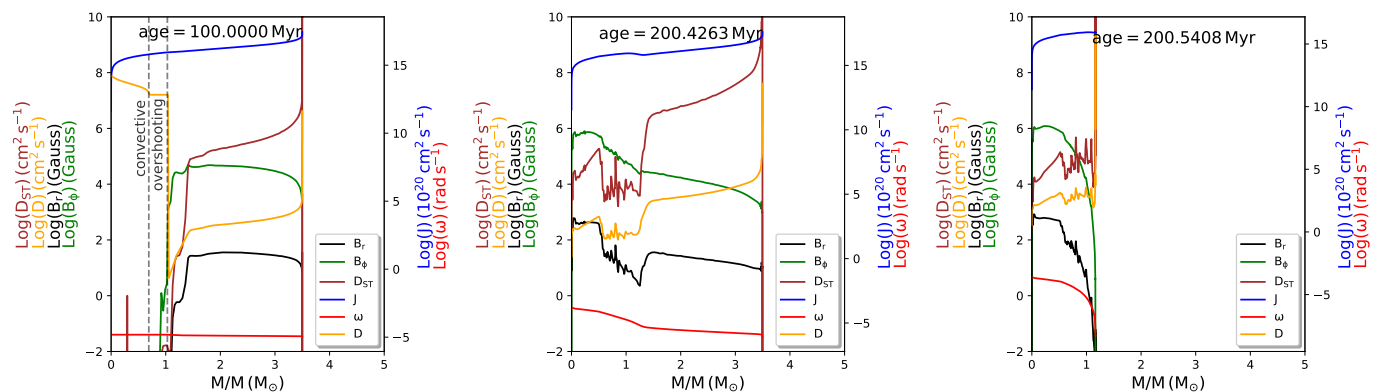


Fig. 18. Profiles of magnetic fields generated by the Tayler-Spruit dynamo in the poloidal B_r and toroidal B_t components for the donor star at different evolutionary stages. The profiles represent the stages of inversion of the ${}^1\text{H}/{}^4\text{He}$ ratio (X₁ stage, left panel), the start of mass transfer (E-stage, middle panel) and the current stage (X₂, right panel). The Eulerian diffusion coefficient for mixing is represented in orange color, the Spruit-Tayler (ST) diffusion coefficient by the brown line, the poloidal magnetic field as a black line, the toroidal magnetic field in green, whereas the angular momentum is represented in blue and the angular velocity in red.

Mennickent R. E., Djurašević G., Vince I., et al., 2020b, *A&A*, 642, A211.

Mennickent R. E., Djurašević G., Petrović J., Gorrini P., Burgos F., Jurković M. I., Magalhaes A. M., et al., 2022, *A&A*, 666, A51.

Mourard D., Brož M., Nemravová J. A., et al., 2018, *A&A*, 618, A112.

Navarrete F. H., Käpylä P. J., Schleicher D. R. G., Banerjee R., 2023, *A&A*, 678, A9.

Paczynski B., 1977, *ApJ*, 216, 822.

Pawlak M., Graczyk D., Soszyński I., et al., 2013, *Acta Astronomika*, 63, 323.

Poleski R., Soszyński I., Udalski A., et al., 2010, *Acta Astronomika*, 60, 179.

Pawlak M., Soszyński I., Udalski A., Szymański M. K., Wyrzykowski Ł., Ulaczyk K., Poleski R., et al., 2016, *Acta Astronomika*, 66, 421.

Ritter H., 1988, *A&A*, 202, 93.

Rojas García G., Mennickent R., Iwanek P., Gorrini P., Garcés J., Soszyński I., Astudillo-Defru N., 2021, *ApJ*, 922, 30.

Rosales Guzmán J. A., Mennickent R. E., Djurašević G., Araya I., Curé M., 2018, *MNRAS*, 476, 3039

Rosales J. A., Mennickent R. E., Djurašević G., Schleicher D. R. G., Zharikov S., Araya I., Celedón L., et al., 2021, *AJ*, 162, 66.

Rosales J. A., Mennickent R. E., Djurašević G., Araya I., Curé M., Schleicher D. R. G., Petrović J., 2023, *A&A*, 670, A94.

Paxton B., Bildsten L., Dotter A., Herwig F., Lesaffre P., Timmes F., 2011, *ApJS*, 192, 3.

Paxton B., Marchant P., Schwab J., Bauer E. B., Bildsten L., Cantiello M., Dessart L., et al., 2015, *ApJS*, 220, 15.

San Martín-Pérez R. I., Schleicher D. R. G., Mennickent R. E., Rosales J. A., 2019, *Boletín de la Asociación Argentina de Astronomía*, 61, 107.

Schleicher, D. R. G., & Mennickent, R. E. 2017, *A&A*, 602, A109.

Skowron D. M., Skowron J., Udalski A., Szymański M. K., Soszyński I., Wyrzykowski Ł., Ulaczyk K., et al., 2021, *ApJS*, 252, 23.

Stellingwerf R. F., 1978, *ApJ*, 224, 953.

Sterken C., 2005, *ASP Conference Series*, 335, 3.

Terrell D., Wilson R. E., 2005, *Ap&SS*, 296, 221.

Udalski A., Szymański M. K. & Szymański G. 2015, *Acta Astronomika*, 65, 1.

von Zeipel H., 1924, *MNRAS*, 84, 702.

Warner B., 1995, *Cataclysmic Variable Stars*, Cambridge Astrophysics Series, 28, ISBN: 9780511586491.

Zechmeister M., Kürster M., 2009, *A&A*, 496, 577.

Appendix A: Error estimates

We estimate the errors of mass, radius and orbital separation assuming an uncertainty in the temperature and using an analytical approach. The luminosity of a follows the Stefan-Boltzmann law:

$$L = 4\pi R^2 \sigma T^4 \quad (\text{A.1})$$

where R is the radius of the star, σ is the Stefan-Boltzmann constant and T is the effective temperature. Now, an error in the temperature, ΔT , affects the luminosity due to the dependence $L \propto T^4$. If we make an error ΔT in measuring the effective temperature of the star, the relative error in the luminosity will be:

$$\frac{\Delta L}{L} = 4 \frac{\Delta T}{T} \quad (\text{A.2})$$

Given that for a main sequence star $L \propto M^\alpha$, an error in the luminosity, ΔL , translates into an error in the mass, ΔM , as follows:

$$\frac{\Delta M}{M} = \frac{1}{\alpha} \frac{\Delta L}{L} = \frac{4}{\alpha} \frac{\Delta T}{T} \quad (\text{A.3})$$

If we use $\alpha \approx 3.5$ for a main sequence star, and consider that for a giant star the exponent should be larger because of the increasing radius, the relative error in the mass of the donor would be:

$$\frac{\Delta M}{M} < \frac{4}{3.5} \frac{\Delta T}{T} \approx 1.14 \frac{\Delta T}{T} \quad (\text{A.4})$$

On the other hand, the orbital separation in a binary system is given by Kepler's third law:

$$a = \left(\frac{G(M_1 + M_2)P^2}{4\pi^2} \right)^{1/3} \quad (\text{A.5})$$

An error in the stellar masses affects the orbital separation as follows:

$$\frac{\Delta a}{a} = \frac{1}{3} \frac{\Delta(M_1 + M_2)}{M_1 + M_2} \quad (\text{A.6})$$

Assuming the relative error is similar for both stars, we can write:

$$\frac{\Delta a}{a} = \frac{1}{3} \frac{4}{\alpha} \frac{\Delta T}{T} \quad (\text{A.7})$$

For $\alpha > 3.5$:

$$\frac{\Delta a}{a} < \frac{1.14}{3} \frac{\Delta T}{T} \approx 0.38 \frac{\Delta T}{T} \quad (\text{A.8})$$

From the above equations, and assuming a temperature uncertainty of 4%, we get masses with uncertainty less than 5% and orbital separation with uncertainty less than 2%.

To calculate the error in the radius of the giant star filling its Roche lobe, we need to consider how the errors in the mass ratio ($q = M_1/M_2$) and the orbital separation (a) affect the error in the Roche lobe radius (R_L).

Recall that the Roche lobe radius is given by the empirical Eggleton formula:

$$\frac{R_L}{a} = \frac{0.49q^{2/3}}{0.6q^{2/3} + \ln(1 + q^{1/3})} \quad (\text{A.9})$$

To find the error in R_L (the Roche lobe radius, which will approximately be the radius of the giant star), we will apply the formula for error propagation. This will allow us to calculate the error in R_L as a function of the errors in q and a .

Since R_L depends on two variables q and a , the error in R_L , denoted as ΔR_L , can be computed using the following error propagation formula:

$$\frac{\Delta R_L}{R_L} = \sqrt{\left(\frac{\partial R_L}{\partial q} \cdot \frac{\Delta q}{q} \right)^2 + \left(\frac{\partial R_L}{\partial a} \cdot \frac{\Delta a}{a} \right)^2} \quad (\text{A.10})$$

First we calculate the partial derivative with respect to q :

$$\frac{\partial}{\partial q} \left(\frac{R_L}{a} \right) = \frac{0.49 \cdot \frac{2}{3} q^{-1/3}}{(0.6q^{2/3} + \ln(1 + q^{1/3}))} - \frac{0.49q^{2/3} \cdot \left(0.6 \cdot \frac{2}{3} q^{-1/3} + \frac{1}{3(1+q^{1/3})q^{2/3}} \right)}{(0.6q^{2/3} + \ln(1 + q^{1/3}))^2} \quad (\text{A.11})$$

Then, we calculate the partial derivative with respect to a . The dependence of R_L on a is straightforward, as $R_L \propto a$. Thus:

$$\frac{\partial R_L}{\partial a} = \frac{R_L}{a} \quad (\text{A.12})$$

For $q = 0.19$ with an associated error of 0.02, and assuming a 4% relative error in the orbital separation, we obtain a relative error of 3.54% for the Roche Lobe radius, which also corresponds to the donor star's radius.

If the gainer follows a mass-radius relationship $M \propto R^\beta$ with β between 0.57 and 0.7, we get the fractional error in the gainer radius less than 0.7 times the fractional error in the gainer mass. If this last is 5%, then the gainer fractional radius uncertainty is less than 4%.

Finally, the surface gravity in solar units is given by:

$$\log g = \log \left(\frac{M}{R^2} \right) + \log g_\odot \quad (\text{A.13})$$

where $\log g_\odot$ is the solar surface gravity. The error is given by:

$$\Delta(\log g) = \sqrt{\left(\frac{\Delta M}{M \ln(10)} \right)^2 + \left(\frac{2\Delta R}{R \ln(10)} \right)^2} \quad (\text{A.14})$$

Using the fractional errors quoted above, we derive the errors for $\log g$ given in Table 3.

Appendix B: Additional material

Table B.1. Epochs of main eclipses (HJD - 2450000).

Epoch	Epoch	Epoch	Epoch	Epoch
-1169.6891	506.9281	4896.5155	5926.7238	8444.7825
-522.0847	1119.0054	4896.5829	5927.7229	8445.6026
-407.8935	2644.7548	4896.6069	5964.6214	8445.7437
-407.7107	2682.7154	4934.4964	5965.6203	8445.8333
-406.9255	2911.8491	4935.4862	6002.5849	9856.8030
-369.7454	2950.6943	5850.7912	6003.5510	9856.8183
-368.9330	3408.6229	5851.8002	7339.7611	9856.8330
-368.7462	3446.5358	5888.7934	7453.6087	9856.8470
-331.8936	4399.7700	5889.8355	8444.5994	9895.6433
432.0125	4476.6967	5925.7121	8444.6805	9895.6574
9895.6717	9933.6693	9971.6538	10009.5486	10010.5759
9895.6857	9933.7353	9971.6684	10009.5626	10010.5951
9895.7001	9933.7498	9971.6845	10009.5824	10010.6170
9895.7142	9971.5522	9971.6986	10009.5970	10010.6311
9895.7286	9971.5665	9971.7129	10009.6159	10010.6454
9932.7679	9971.5805	9971.7268	10009.6299	
9932.7961	9971.5948	9971.7411	10009.6444	
9933.5796	9971.6088	9971.7552	10010.5153	
9933.6407	9971.6235	10009.5153	10010.5296	
9933.6548	9971.6397	10009.5293	10010.5442	

Table B.2. Parameters of the light curve fits.

set	F_d ± 0.01	T_{disc} ± 60 (K)	A_{hs} ± 0.04	θ_{hs} ± 1.2 ($^\circ$)	λ_{hs} ± 3.0 ($^\circ$)	θ_{rad} ± 3.0 ($^\circ$)	A_{bs} ± 0.04	θ_{bs} ± 1.3 ($^\circ$)	λ_{bs} ± 8.0 ($^\circ$)	a_T ± 0.02	R_{disk} ± 0.1 (R_\odot)	d_e ± 0.1 (R_\odot)	d_c ± 0.2 (R_\odot)
01	0.886	3475	1.36	16.8	328.0	-5.1	1.13	44.4	101.8	0.74	42.99	6.68	3.77
02	0.898	3258	1.24	16.7	347.8	17.1	1.16	45.6	161.2	0.75	43.56	9.52	4.43
03	0.888	3432	1.27	20.3	345.2	-8.6	1.08	38.8	169.6	0.75	43.10	8.14	4.47
04	0.866	3418	1.21	19.3	337.5	-3.2	1.09	40.5	155.0	0.75	42.00	8.57	4.51
05	0.903	3391	1.23	22.1	341.2	3.3	1.15	39.3	162.3	0.74	43.81	9.09	4.64
06	0.749	3985	1.20	25.4	332.1	-2.8	1.12	34.7	93.7	0.49	36.35	9.03	3.46
07	0.747	3745	1.13	21.9	348.0	16.9	1.09	32.8	59.7	0.73	36.26	9.04	4.67
08	0.724	3678	1.07	23.5	349.1	25.5	1.07	36.9	61.3	0.74	35.13	10.21	5.02
09	0.839	3600	1.35	16.7	328.6	-2.3	1.14	48.4	81.4	0.72	42.12	6.54	3.81
10	0.752	3729	1.30	17.5	340.0	5.1	1.19	48.1	77.1	0.75	36.47	6.47	4.46
11	0.710	3802	1.33	18.1	333.2	6.5	1.21	48.2	75.1	0.75	34.20	6.20	4.42
12	0.753	3664	1.26	14.7	316.3	-31.5	1.18	42.0	59.1	0.74	36.55	7.06	4.53
13	0.762	3585	1.30	15.2	310.7	-2.3	1.16	41.8	55.2	0.73	36.98	8.32	4.53
14	0.772	3739	1.39	19.7	310.5	12.9	1.18	49.9	92.7	0.75	37.44	10.73	4.54
15	0.726	3681	1.39	22.0	317.7	6.5	1.18	44.0	98.0	0.75	35.20	10.40	4.54
16	0.736	3648	1.40	20.8	322.2	-12.2	1.16	43.6	98.9	0.74	35.71	9.83	4.45
17	0.872	3692	1.38	17.4	313.1	4.9	1.12	49.4	118.1	0.72	42.32	6.40	3.61
18	0.881	3602	1.35	19.7	323.0	1.2	1.21	50.5	64.0	0.72	42.73	6.07	3.06
19	0.865	3522	1.18	15.1	325.6	-13.6	1.15	47.4	66.9	0.69	41.96	7.35	3.37
20	0.896	3545	1.34	16.9	328.5	-12	1.18	48.7	66.7	0.75	43.48	6.89	3.75
21	0.756	3851	1.21	15.2	316.0	18.4	1.07	35.2	102.4	0.70	36.66	10.9	4.53
22	0.756	3863	1.27	15.9	318.5	22.8	1.08	36.1	106.1	0.73	36.70	9.76	4.51
23	0.729	3847	1.28	16.4	326.9	28.7	1.08	39.1	82.1	0.74	35.36	10.48	4.53
24	0.659	4217	1.30	15.9	310.6	11.3	1.10	42.9	106.0	0.72	31.97	12.86	4.09
25	0.677	4114	1.28	16.0	316.8	-9.2	1.15	47.9	79.6	0.67	32.84	9.62	3.38
26	0.699	3846	1.39	18.2	321.9	1.1	1.16	50.4	91.7	0.74	33.90	9.89	3.71
27	0.732	3902	1.21	25.1	326.5	-11.6	1.13	35.4	66.7	0.69	35.54	10.01	4.41
Mean	0.786	3697	1.282	18.6	327.2	2.5	1.138	43.0	94.5	0.72	38.20	8.74	4.19
std	0.077	220	0.085	3.1	12.1	13.9	0.043	5.5	33.3	0.05	3.81	1.78	0.50

Note: Light curve fit parameters with their formal errors for the datasets. Mean and standard deviation are also given. See text for details.